

## Research Paper

## A Rattle Signal Denoising and Enhancing Method Based on Wavelet Packet Decomposition and Mathematical Morphology Filter for Vehicle

Linyuan LIANG<sup>(1),(2)</sup>, Shuming CHEN<sup>(1),(2)\*</sup>, Peiran LI<sup>(1)</sup><sup>(1)</sup> State Key Laboratory of Vehicle NVH and Safety Technology  
Chongqing 401122, China<sup>(2)</sup> State Key Laboratory of Automotive Simulation and Control, Jilin University  
Changchun 130022, China

\*Corresponding Author e-mail: smchen@jlu.edu.cn

(received August 9, 2021; accepted January 31, 2022)

Buzz, squeak and rattle (BSR) noise has become apparent in vehicles due to the significant reductions in engine noise and road noise. The BSR often occurs in driving condition with many interference signals. Thus, the automatic BSR detection remains a challenge for vehicle engineers. In this paper, a rattle signal denoising and enhancing method is proposed to extract the rattle components from in-vehicle background noise. The proposed method combines the advantages of wavelet packet decomposition and mathematical morphology filter. The critical frequency band and the information entropy are introduced to improve the wavelet packet threshold denoising method. A rattle component enhancing method based on multi-scale compound morphological filter is proposed, and the kurtosis values are introduced to determine the best parameters of the filter. To examine the feasibility of the proposed algorithm, synthetic brake caliper rattle signals with various SNR ratios are prepared to verify the algorithm. In the validation analysis, the proposed method can well remove the disturbance background noise in the signal and extract the rattle components with well SNR ratios. It is believed that the algorithm discussed in this paper can be further applied to facilitate the detection of the vehicle rattle noise in industry.

**Keywords:** rattle signals; wavelet packet decomposition; mathematical morphology filter; critical frequency band; information entropy.



Copyright © 2022 L. Liang *et al.*  
This is an open-access article distributed under the terms of the Creative Commons Attribution-ShareAlike 4.0 International (CC BY-SA 4.0 <https://creativecommons.org/licenses/by-sa/4.0/>) which permits use, distribution, and reproduction in any medium, provided that the article is properly cited, the use is non-commercial, and no modifications or adaptations are made.

## 1. Introduction

A vehicle interior noise is one of the most important factors that affects the customers' perception of the vehicle quality. The vehicle interior noise may be roughly divided into two categories: the persistent type and the transient or come-and-go style (TRAPP, FANG, 2012; LIANG *et al.*, 2020a). Persistent noise such as engine or road boom noise or wind noise will occur constantly during wide-ranging operation conditions. It is annoying and discomforting to customers, and should be eliminated primarily. With recent significant reductions in the persistent type of noise, the come-and-go kind of noise, including the buzz, squeak and rattle noise, becomes more apparent and needs to be elimi-

nated to further improve the vehicle quality (CHOI *et al.*, 2013; CHAUDHARI *et al.*, 2018; SHIN, CHEONG, 2010; LIANG *et al.*, 2020b).

BSR may occur at any two contact surfaces that can have relative motions in vehicle. It is an issue involving various components and systems in vehicle. Rattle, the impact-induced noise, accounts for most of the BSR issues in vehicle (DUAN *et al.*, 2020; LIANG *et al.*, 2021a). It is a type of broad-band frequency noise with the majority content at low frequency. It is generated by the low frequency vibration contact.

In general, BSR noises may have very low SNR ratios even under normal operating condition. Furthermore, masking will also occur when the perception of a sound is affected by the presence of another sound

(LIANG *et al.*, 2021b). All these factors make it a challenge for the detection of the BSR noises. Thus, it is necessary to introduce an effective signal denoising method to extract the rattle components in the signal. Generally, wavelet packet analysis can meet the requirements of rattle signal denoising and extraction. The idea behind the wavelet packet denoising is layered noise reduction. It can ensure that the noise is suppressed while retaining the effective components in the signal to achieve better SNR ratios. HASHIM *et al.* (2020) used Shannon entropy to select the best basis function for the wavelet packet decomposition. And the optimal decomposition level of wavelet packet decomposition was determined by the ratio of the maximum energy to the Shannon entropy of each layer decomposition coefficient. YUE *et al.* (2019) proposed a Bayesian wavelet packet denoising method based on the minimum mean square error. Besides, they constructed an index based on kurtosis and skewness to determine the best wavelet packet decomposition levels. The proposed method was successfully used in the analysis of track fault signals. ZHANG *et al.* (2021) proposed a wavelet packet decomposition noise reduction method based on Teager energy operator and kurtosis, which can effectively detect the impact component in the signal. The proposed method was applied to the bearing fault diagnosis successfully. HUANG *et al.* (2016) also introduced wavelet packet transform to extract the squeak and rattle feature of the suspension shock absorber. Most of these applications and optimization methods are suitable for the noise reduction of low-frequency noise or Gaussian noise. However, the background noises of rattle signals are always the broadband in-vehicle noises. The overlapping frequency bands of the in-vehicle noises and the rattle signals are relatively wide, thus the separation is difficult.

Based on the characteristics of rattle signal and the background noise in vehicle, a rattle signal denoising and enhancing method based on wavelet packet decomposition and mathematical morphology filter is proposed in this paper. The proposed method includes the denoising process and the signal enhancing process. Here, we present a brief workflow of the proposed signal denoising and enhancing strategy. As illustrated in Fig. 1, the noise signal is decomposed by the improved wavelet packet decomposition firstly. The decomposition structure of the improved wavelet packet decomposition method is under the guidance of critical frequency band. After the decomposition, the improved wavelet packet thresholding method based on information entropy is performed on the wavelet packet coefficients. Then the reconstructed signal can be obtained. To further improve the SNR ratio of the signal, the multi-scale compound mathematical morphological filter is established to enhance the processed signal. The proposed method is verified with synthesized rattle signal with various SNRs levels.

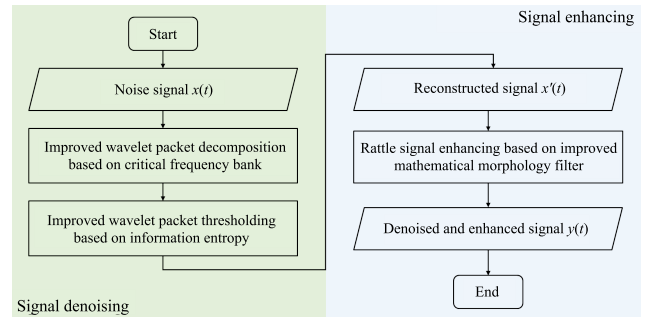


Fig. 1. The workflow of the proposed rattle signal denoising and enhancing strategy.

## 2. Improved wavelet packet thresholding method

Rattle noises often occur under strong background noise in vehicles. To remove the undesired noises, several signal processing methods have been introduced and achieved ideal results. These methods include the discrete wavelet transform (BI *et al.*, 2019; LIANG *et al.*, 2020a), the empirical wavelet decomposition (EWD) (CHEN, SONG, 2018; PAN *et al.*, 2016), empirical mode decomposition method (EMD) and so on (YANG *et al.*, 2015; YASLAN, Bican, 2017). Nevertheless, few methods are verified to be effective to preserve the impact characteristic and remove the in-vehicle background noises. In this study, we propose a wavelet packet denoising method based on critical frequency band and information entropy.

### 2.1. Basic theory of wavelet packet decomposition

Wavelet transform is a mathematical tool efficiently used in non-stationary signal processing. It converts a signal into a different form with the goal to reveal the characteristics or ‘features’ hidden within the original signal and represent the original signal more succinctly (GAO, YAN, 2011a). A basic wavelet function is needed in order to realize the wavelet transform. These wavelet functions are small waves that have oscillating wavelike characteristics and have their energy concentrated in time. A set of wavelets is called a wavelet family. It is a family of orthogonal functions which can be obtained as Eq. (1)

$$\psi_{s,\tau}(t) = \frac{1}{\sqrt{s}} \psi\left(\frac{t-\tau}{s}\right), \quad s > 0, \quad \tau \in \mathbb{R}, \quad (1)$$

where  $s$  and  $\tau$  are the scale factor and the translation factor, respectively, and  $\mathbb{R}$  is the set of real numbers.  $\frac{2}{\sqrt{s}}$  ensures that the energy of the wavelet family will remain the same under different scales.

Given a finite-energy signal  $x(t)$ , the continuous wavelet transform of the signal  $x(t)$  can be defined as

$$W_{s,\tau}(t) = \frac{1}{\sqrt{|s|}} \int_{-\infty}^{\infty} x(t) \psi\left(\frac{t-\tau}{s}\right) dt. \quad (2)$$

To obtain the discrete wavelet transform (DWT), we need to discretize the scale factor and the translation factor (GAO, YAN, 2011b; WANG *et al.*, 2007; XING *et al.*, 2016). This type of discretization is expressed as

$$\begin{cases} s = s_0^j, \\ \tau = k\tau_0, \end{cases} \quad s_0 < 1, \quad \tau_0 \neq 0, \quad j \in \mathbb{Z}, \quad k \in \mathbb{Z}, \quad (3)$$

where  $\mathbb{Z}$  is the set of integers.

The corresponding family of the basic wavelet is then expressed as

$$\psi_{j,k}(t) = \frac{1}{\sqrt{s_0^j}} \psi\left(\frac{t - k\tau_0 s_0^j}{s_0^j}\right). \quad (4)$$

Generally,  $s_0 = 2$  and  $\tau_0 = 1$  (ADDISON, 2002). Consequently, the wavelet function can be expressed as

$$\psi_{j,k}(t) = \frac{1}{\sqrt{2^j}} \psi\left(\frac{t - k2^j}{2^j}\right). \quad (5)$$

As a consequence, the discrete wavelet transform of the given signal  $x(t)$  can be acquired as

$$\begin{aligned} W_{j,k}(t) &= \langle x(t), \psi_{j,k}(t) \rangle \\ &= \frac{1}{\sqrt{2^j}} \int_{-\infty}^{\infty} x(t) \psi^*\left(\frac{t - k2^j}{2^j}\right) dt, \end{aligned} \quad (6)$$

where the symbol  $\langle \cdot \rangle$  refers to the inner product operation.

The signal  $x(t)$  can be reconstructed through the inverse discrete wavelet transform as

$$x(t) = \sum_{j=-\infty}^{\infty} \sum_{k=-\infty}^{\infty} W_{j,k}(t) \psi_{j,k}(t). \quad (7)$$

While discrete wavelet transform provides flexible time-frequency resolution, it suffers from a relatively low resolution in the high-frequency region. This deficiency leads to difficulty in differentiating high-frequency transient components. The wavelet packet transform (WPT), in comparison, further decomposes the detailed information of the signal in the high-frequency region, thereby overcoming this limitation.

The wavelet packet is expressed as

$$\begin{cases} u_{2n}^{(j)}(t) = \sqrt{2} \sum_k h(k) u_n^{(j)}(2t - k), \\ u_{2n+1}^{(j)}(t) = \sqrt{2} \sum_k g(k) u_n^{(j)}(2t - k), \end{cases} \quad (8)$$

where  $u_0^{(0)}(t) = \phi(t)$  is the scaling function, and  $u_1^{(0)}(t) = \psi(t)$  is the wavelet function;  $j$  denotes the  $j$ -th level of the wavelet packet decomposition, and there will be  $2^j$  wavelet packet sub-bands at the  $j$ -th level;  $h(k)$  is the scale filter which is a low-pass filter, and  $g(k)$  is the wavelet filter which is a high-pass filter.

Here specifies the wavelet packet  $\{u_n(t) | n \in \mathbb{Z}^+\}$ . The orthogonal basis can be given by

$$\{u_{j,m,n}(t) = 2^{j/2} u_m(2^j t - m) | j, m \in \mathbb{Z}^+\},$$

where  $j$ ,  $m$ , and  $n$  are the scale, translation, and the oscillation parameters, respectively, and  $\mathbb{Z}^+$  is the set of positive integers. The decomposed coefficients of the signal  $x(t)$  can be defined as  $C_m^{j,n} = \{C_m^{j,n}\}_{m \in \mathbb{Z}^+}$ , and  $C_m^{j,n} = \langle x, u_{j,m,n} \rangle$ . Therefore, the wavelet packet decomposition of the signal can also be defined as

$$\begin{cases} C_m^{j,2n} = \sum_{k=-\infty}^{\infty} h_{2m-k}^* C_k^{j+1,n}, \\ C_m^{j,2n+1} = \sum_{k=-\infty}^{\infty} g_{2m-k}^* C_k^{j+1,n}. \end{cases} \quad (9)$$

Conversely, the reconstruction formula of the wavelet packet can be expressed as

$$C_m^{j+1,n} = \sum_{k=-\infty}^{\infty} h_{2m-k} C_k^{j,2n} + \sum_{k=-\infty}^{\infty} g_{2m-k} C_k^{j,2n+1}. \quad (10)$$

The structure of the wavelet packet decomposition tree can be manually designed by splitting or combining some nodes from a complete wavelet packet decomposition tree according to the aim of the research or some particular requirements.

## 2.2. Improved wavelet packet decomposition

The rattle signals often cover a wide frequency range, such as the background noise in vehicles. The audible background noise in vehicles includes the low-frequency road noise and wind noise, high-frequency motors noises, and electrical equipment noises. In this study, an improved wavelet packet decomposition method based on the critical frequency band is proposed. The frequency characteristics of the sub-signals decomposed by the improved wavelet packet decomposition method are more in line with the subjective perception of sound by the human ear.

In this section, the optimal subtree of an initial wavelet packet decomposition tree with respect to the critical bank criterion is designed. The one-third octave is introduced to substitute the critical bands assuming the human auditory system (XING *et al.*, 2016). The first step to construct the decomposition method is to choose the sample rate of the signal. In this study, the sampling rate was chosen to be 48 kHz. Within this bandwidth, there are approximately 21 critical bands that cover the audible frequency range of 20 Hz – 20 kHz. The specific process of the improved wavelet packet decomposition is described as follows:

*Step 1:* The selection of wavelet packet decomposition parameters: in this study, the “db5” wavelet basis function was chosen to carry out 6-layer wavelet packet decomposition on the signal. The complete wavelet packet decomposition tree can be obtained. The frequency range of each sub-band of the decomposed signal is 375 Hz.

*Step 2:* The establishment of the optimal wavelet packet decomposition structure: based on the bandwidth characteristics of the critical frequency band, the optimal wavelet packet decomposition structure was designed. Figure 2 shows the optimal wavelet packet decomposition tree.

*Step 3:* Rearrangement of the wavelet packet nodes: in the wavelet packet decomposition, the frequency ranges of the decomposition nodes do not completely follow the order from small to large. The sequence

of the wavelet packet nodes follows the sequence of the Gray code (YING, JIN-YAN, 2007). Thus, the frequency-band of the wavelet packet nodes needs to be adjusted in sequence. Table 1 shows the approximate frequency range of the rearranged nodes and the correspondence between wavelet packet nodes and the critical frequency band.

As can be seen in Fig. 2 and Table 1, the first 36 wavelet packet decomposition nodes are grouped into 21 sub-signals based on the frequency range of the cri-

Table 1. Approximate frequency ranges of the modified wavelet.

| No. | Original nodes | Rearranged nodes | Critical band rate (Bark) | Approximate frequency ranges [Hz] | Critical bands of the 1/3 octaves [Hz] | Center frequency of the 1/3 octaves [Hz] |
|-----|----------------|------------------|---------------------------|-----------------------------------|--|--|
| 1   | (8,0)          | (8,0)            | 1                         | 20–93.75                          | 20–90                                  | 25, 32, 40, 50, 63, 80                   |
| 2   | (8,1)          | (8,1)            | 2                         | 93.75–187.5                       | 90–180                                 | 100, 125, 160                            |
| 3   | (8,2)          | (8,3)            | 3                         | 187.5–281.25                      | 180–280                                | 200, 250                                 |
| 4   | (8,3)          | (8,2)            | 4                         | 281.25–375                        | 280–355                                | 315                                      |
| 5   | (9,8)          | (8,6)            | 5                         | 375–468.75                        | 355–447                                | 400                                      |
| 6   | (9,9)          | (8,7)            | 6                         | 468.75–562.5                      | 447–562                                | 500                                      |
| 7   | (8,5)          | (8,5)            | 7                         | 526.5–703.125                     | 562–708                                | 630                                      |
| 8   | (8,6)          | (9,9)            |                           |                                   |  |  |
| 9   | (8,7)          | (9,8)            | 8                         | 703.125–843.75                    | 708–891                                | 800                                      |
| 10  | (8,8)          | (8,12)           |                           |                                   |  |  |
| 11  | (8,9)          | (8,13)           | 9                         | 843.75–1125                       | 891–1120                               | 1000                                     |
| 12  | (7,5)          | (7,7)            |                           |                                   |  |  |
| 13  | (8,12)         | (7,5)            | 10                        | 1125–1406.25                      | 1120–1410                              | 1250                                     |
| 14  | (8,13)         | (8,9)            |                           |                                   |  |  |
| 15  | (7,7)          | (8,8)            | 11                        | 1406.25–1875                      | 1410–1780                              | 1600                                     |
| 16  | (7,8)          | (7,12)           |                           |                                   |  |  |
| 17  | (7,9)          | (7,13)           |                           |                                   |  |  |
| 18  | (6,5)          | (6,7)            | 12                        | 1875–2250                         | 1780–2240                              | 2000                                     |
| 19  | (7,12)         | (6,5)            | 13                        | 2250–2,812.5                      | 2240–2820                              | 2500                                     |
| 20  | (7,13)         | (7,9)            |                           |                                   |  |  |
| 21  | (6,7)          | (7,8)            | 14                        | 2812.5–3562.5                     | 2820–3550                              | 3150                                     |
| 22  | (5,4)          | (6,12)           |                           |                                   |  |  |
| 23  | (5,5)          | (7,27)           |                           |                                   |  |  |
| 24  | (6,12)         | (7,26)           | 15                        | 3562.5–4500                       | 3550–4470                              | 4000                                     |
| 25  | (7,26)         | (5,7)            |                           |                                   |  |  |
| 26  | (7,27)         | (5,5)            | 16                        | 4500–6000                         | 4470–5620                              | 5000                                     |
| 27  | (5,7)          | (5,4)            |                           |                                   |  |  |
| 28  | (5,8)          | (5,12)           | 17                        | 6000–7500                         | 5620–7080                              | 6300                                     |
| 29  | (5,9)          | (5,13)           |                           |                                   |  |  |
| 30  | (4,5)          | (4,7)            | 18                        | 7500–9000                         | 7080–8910                              | 8000                                     |
| 31  | (5,12)         | (4,5)            | 19                        | 9000–11250                        | 8910–11200                             | 10000                                    |
| 32  | (5,13)         | (5,9)            |                           |                                   |  |  |
| 33  | (4,7)          | (5,8)            | 20                        | 11250–13500                       | 11200–14100                            | 12500                                    |
| 34  | (2,2)          | (4,12)           |                           |                                   |  |  |
| 35  | (4,12)         | (4,13)           | 21                        | 13500–18000                       | 14100–17800                            | 16000                                    |
| 36  | (4,13)         | (3,7)            |                           |                                   |  |  |
| 37  | (3,7)          | (2,2)            | \                         | \                                 | \                                      | \  |

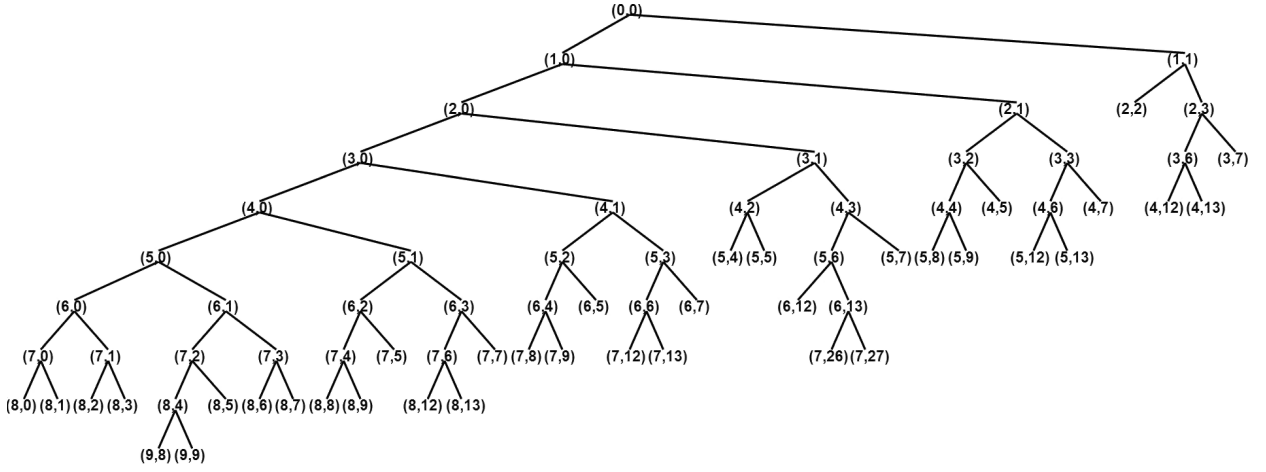


Fig. 2. The structure of the wavelet packet decomposition tree.

tical frequency bands and the wavelet packet decomposition nodes. Table 1 shows the results of wavelet packet node division and the corresponding frequency range. Among them, (8,0), (8,1), (8,3), (8,2), (8,6), and (8,7) correspond to the first six critical frequency bands ( $z = 1, 2, 3, 4, 5, 6$ ). The seventh critical band is composed of node signals (8,5) and (9,9), and the eighth critical band is composed of node signals (9,8) and (8,12).

### 2.3. Improved wavelet packet thresholding

The selection of threshold function and threshold in wavelet packet denoising directly influences the denoising effect. If the threshold is too large, the rattle components will be filtered out as noise. On the contrary, if the threshold is too small, the noise reduction effect will be poor, which will impair the accuracy of the rattle signal detection.

Traditionally, there are four methods for the threshold estimation, namely the general threshold based on sqtwolog criterion, the heuristic stein unbiased risk threshold based on heursure criterion, the stein unbiased risk threshold based on rigrsure criterion, and the minimaxi threshold based on maximum and minimum criterion. The general sqtwolog criterion threshold proposed by DONOHO (1995) is currently the most commonly used threshold. The expression of the sqtwolog criterion threshold is defined as

$$\lambda = \sigma_u \sqrt{2 \ln(N)}, \quad (11)$$

where  $N$  is the length of the noise signal, and  $\sigma_u$  is the standard deviation of the noise signal. The expression of  $\sigma_u$  is shown as

$$\sigma_u = \frac{\text{median}(|d_j(k)|)}{0.6745}, \quad (12)$$

where  $\text{median}(\cdot)$  refers to the median operation,  $j$  refers to the decomposition scale of the wavelet packet,

and  $d_j(k)$  is the decomposition coefficient of the  $k$ -th wavelet packet in the  $j$ -th layer of the wavelet packet decomposition.

The sqtwolog criterion-based threshold calculation method mainly pays attention to the standard deviation and the length of the signal, ignoring the characteristic of the rattle component in the signal. Thus, this thresholding method cannot adjust the threshold value adaptively. In this study, the information entropy is introduced to improve the sqtwolog criterion thresholding method.

The concept of information entropy was proposed by SHANNON (1948). For the discrete 1-D signals, information entropy describes the complexity of the signal and the amount of information it contains. For example, the noise signals usually have high entropy, since they carry little new information and many similar sequences. Conversely, the BSR signals have lower entropy because of the occurrences of new patterns. In other words, the information entropy has the capacity to indicate the BSR component in the signal. Given a discrete signal  $x(n)$ , the information entropy is defined as

$$I = - \sum_{i=1}^n P_i \log(P_i), \quad (13)$$

where  $P(x_i)$  is the probability of possible events, and  $n$  is the number of events.

The thresholding method based on the information entropy is defined as

$$\lambda = \frac{\alpha \cdot I}{\left(\sigma_u \sqrt{2 \ln(N)}\right)^\beta}, \quad (14)$$

where  $I$  is the information entropy,  $N$  is the length of the noise signal,  $\sigma_u$  is the standard deviation of the noise signal,  $\alpha$  and  $\beta$  are adjustment factors. In this study,  $\alpha = 0.8$ ,  $\beta = 2$ .

The modified threshold can adaptively adjust the threshold based on the information entropy of the signal.

The traditional threshold function includes the soft threshold and hard threshold function. Figure 3 shows the curves of soft threshold function and hard threshold function.

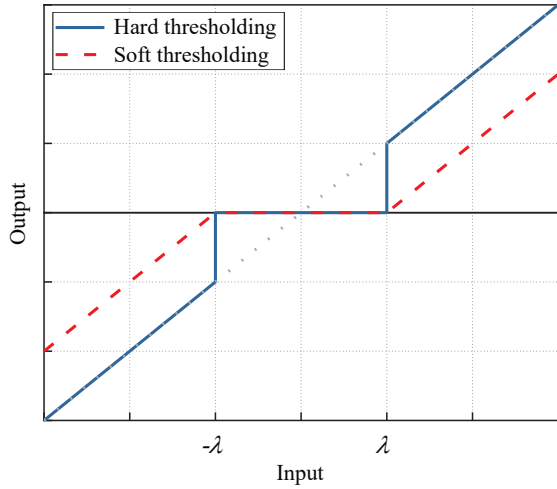


Fig. 3. The curves of the hard and soft thresholding function.

The hard threshold function completely keeps the parts where the absolute value of the wavelet packet coefficient is greater than the threshold, and sets the parts to zeros where the absolute value of the wavelet packet coefficient is less than the threshold. The hard threshold function is defined as

$$\widehat{w}_{j,k} = \begin{cases} w_{j,k}, & |w_{j,k}| \geq \lambda, \\ 0, & |w_{j,k}| < \lambda. \end{cases} \quad (15)$$

The soft-threshold function shrinks and keeps the part where the absolute value of the wavelet packet coefficient is greater than the threshold, and sets the parts to zero where the absolute value of the wavelet packet coefficient is less than the threshold. The soft threshold function can be defined as

$$\widehat{w}_{j,k} = \begin{cases} \text{sign}(w_{j,k}) (|w_{j,k}| - \lambda), & |w_{j,k}| \geq \lambda, \\ 0, & |w_{j,k}| < \lambda, \end{cases} \quad (16)$$

where  $\lambda$  is the threshold,  $w_{j,k}$  is the wavelet packet coefficient,  $\widehat{w}_{j,k}$  is the thresholded wavelet packet coefficient, and  $\text{sign}(\cdot)$  is the sign function.

The hard threshold function is discontinuous at the threshold value, which will cause the reconstructed signal to oscillate. The soft thresholding method is prone to produce excessive smoothing to the signal which will lead to the loss of some high-frequency information.

In order to overcome the above shortcomings of the threshold function, an improved wavelet packet thresholding method based on information entropy is proposed in this study. The optimized threshold function achieves the goal to adjust the thresholding strategy with respect to the information entropy of the signal.

The optimized threshold function is defined as

$$\widehat{w}_{j,k} = \begin{cases} w_{j,k} - (1 - I) \cdot \text{sign}(w_{j,k}) \left( \frac{\lambda^{\frac{1}{1-I}}}{|w_{j,k}|^{\frac{1}{1-I}}} \right), & |w_{j,k}| \geq \lambda, \\ I \cdot \text{sign}(w_{j,k}) \left( \frac{|w_{j,k}|^{\frac{1}{1-I}+1}}{\lambda^{\frac{1}{1-I}}} \right), & |w_{j,k}| < \lambda, \end{cases} \quad (17)$$

where  $\text{sign}(\cdot)$  is the sign function,  $w_{j,k}$  is the wavelet packet coefficient,  $\widehat{w}_{j,k}$  is the thresholded coefficient,  $\lambda$  is the threshold,  $I$  is the normalized information entropy within range (0, 1].

Figure 4 shows the curves of the optimized threshold function based on information entropy. Analyzed from Fig. 4, the sequence will be shrunk and attenuated when the wavelet packet coefficient is less than the threshold value. On the contrary, when the wavelet packet coefficient is greater than the threshold value, the signal is shrunk and retained. As mentioned before, the larger the value of  $I$ , the more noise components in the signal, and the cut-off method of the improved threshold function is closer to the hard threshold function, which can better retain high-frequency rattle components. Conversely, the smaller the value of  $I$ , the more rattle information contained in the wavelet packet coefficients, and the improved threshold function is closer to the soft threshold function with stronger contraction ability, which can better smooth the signal. Therefore, the improved threshold function proposed in this study can perform adaptive noise reduction based on the characteristics of the rattle components in the wavelet packet coefficients.

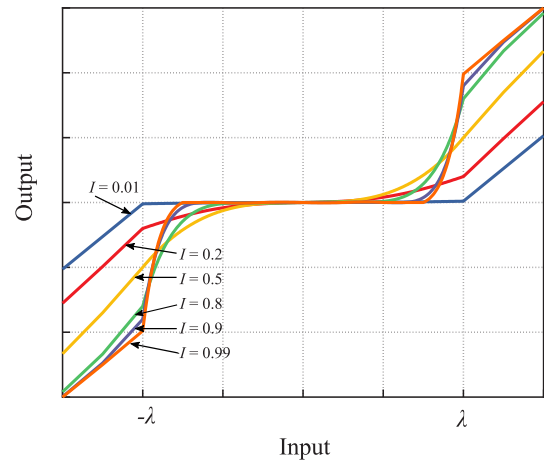


Fig. 4. The curves of the improve threshold function.

After the thresholding, the denoised signal can be obtained by constructing the thresholded wavelet packet coefficients. Generally, the performance of the denoising method can be estimated by the Signal-to-Noise ratio (SNR) of the denoised signal. The SNR is denoted as

$$\text{SNR} = 10 \lg \left( \sum_{i=1}^N \frac{y_i^2}{(\hat{x}_i - y_i)^2} \right). \quad (18)$$

The Root Mean Square Error (RMSE) is also introduced to estimate the performance of the proposed method. The RMSE is denoted as

$$\text{RMSE} = \frac{1}{N} \sqrt{\sum_{i=1}^N |\hat{x}_i - x_i|^2}, \quad (19)$$

where  $N$  represents the data length of the signal,  $y_i$  represents the original signal,  $\hat{x}_i$  represents the denoised signal, and  $x_i$  represents the noise signal.

### 3. Enhancing method based on mathematical morphology filter

#### 3.1. Basic theory of mathematical morphology filter

Mathematical morphology was developed to quantify the mineral characteristics from thin cross sections by Matheron and Serra in 1964 (SERRA, 2008). Subsequently, this work resulted in a novel practical approach, as well as theoretical advancement in image processing and machine vision field (DAVIES, 2012). The mathematical morphological filter (MMF) was derived from mathematical morphology, and it is usually seemed as a nonlinear filter. Mathematical morphological filter is popular in processing binary and gray-tone images. Recently, the mathematical morphology was also introduced to one-dimensional signal processing such as speech signal, EEG signals (XU *et al.*, 2007), power system, seismic data (LI *et al.*, 2016), magnetotelluric data (LI *et al.*, 2020), vibration signal (LI *et al.*, 2017) and many other fields. Mathematical morphology can extract the shock components in time-domain signal with rational computation complexity.

The basic idea behind the MMF is to use a pre-defined segment slide on each trace, and draw conclusion on how this segment fits or rejects the signal. This segment is called the structure element (SE). The structure element used for the 1-D signal is also 1-D type. The widely used structure elements include flat, triangle, semicircle structure element. The two most basic operations in mathematical morphology are erosion and dilation. Here, we hypothesize that the one-dimensional signal is  $\mathbf{F} = [x_1, x_2, \dots, x_N]^T$ , and the structure element is  $\mathbf{G} = [k_1, k_2, \dots, k_M]^T$ . The dilation and the erosion operations can be expressed as

$$\begin{cases} (f \oplus g)(n) = \max_{m=1,2,\dots,M} [f(n-m) + g(m)], \\ \quad n = 1, 2, \dots, (N - M + 1), \\ (f \odot g)(n) = \min_{m=1,2,\dots,M} [f(n+m) - g(m)], \\ \quad n = 1, 2, \dots, (N + M - 1), \end{cases} \quad (20)$$

where  $N > M$ . Symbols  $\oplus$  and  $\odot$  denote the dilation and the erosion operation, respectively.

It can be noticed that the dilation (erosion) process is equivalent to the maximum (minimum) filtering of the signal within the sliding filter window (or the structural element). Thus, the dilation operation is also known as an expansion process, which fills the concave part of the curve. On the contrary, the erosion operation can remove burrs and spikes in the signal.

By combining these two operations, new operations can be produced. The opening operation and closing operation are shown in Eq. (21). The opening operation processes the signal by an erosion operation following a dilation operation. The closing operation is accomplished by carrying out a dilation operation and an erosion operation:

$$\begin{cases} (f \circ g) = (f \odot g) \oplus g, \\ (f \cdot g) = (f \oplus g) \odot g, \end{cases} \quad (21)$$

where the symbol  $\circ$  and  $\cdot$  represent the opening and closing operation, respectively. The opening operation flattens the positive impulses and matches the negative ones, and the closing operation can flatten the negative impulses and matches the positive ones (TANG *et al.*, 2020).

#### 3.2. Multi-scale compound mathematical morphological filter

By performing the opening and closing operations in sequence, the opening-closing (OC) filter and the closing-opening (CO) filter can be obtained (Eq. (22)). To be more specific, the OC filter is accomplished by performing the opening operation first and then the closing operation. The CO filter is achieved by performing the closing operation and then the opening operation:

$$\begin{cases} \text{OC}(f(n)) = (f \circ g \cdot g)(n) \\ \quad = ((f \odot g \oplus g) \oplus g \odot g)(n), \\ \text{CO}(f(n)) = (f \cdot g \circ g)(n) \\ \quad = ((f \oplus g \odot g) \odot g \oplus g)(n). \end{cases} \quad (22)$$

Both the OC and the CO filter can basically filter out the impact components of the signal, while the OC filter decreases out the positive impacts and the CO filter removes the negative impacts. Generally, the CO filter amplifies the output signal while the OC filter results in smaller output (LI *et al.*, 2020). Therefore, the combined morphological filter (CMF) is proposed with the ability to remove the positive and negative impacts in the signal simultaneously. The combined morphological filter is defined as

$$\text{CMF}(f(n)) = \frac{1}{2} [\text{OC}(f(n)) + \text{CO}(f(n))]. \quad (23)$$

It was verified that the single-scale structural element can successfully extract the effective low-frequency signals (LI *et al.*, 2020). Nevertheless, it is

necessary to develop multiscale morphological filters to achieve more effective signal enhancing. Thus, we introduced the scale  $\varepsilon$  to the structure element. The multiscale combined morphological filter (MCMF) can be defined as

$$\begin{aligned} \mathbf{B} &= \text{MCMF}(f(n)) \\ &= \frac{(f \circ \varepsilon g \cdot \varepsilon g)(n) + (f \cdot \varepsilon g \circ \varepsilon g)(n)}{2}, \end{aligned} \quad (24)$$

where

$$\left\{ \begin{aligned} f \circ \varepsilon g(n) &= (f \odot \varepsilon g \oplus \varepsilon g)(n) \\ &= \underbrace{((f \odot g \odot \dots \odot g) \oplus g \oplus \dots \oplus g)}_{(\varepsilon-1)\text{times}}(n), \\ f \cdot \varepsilon g(n) &= (f \oplus \varepsilon g \odot \varepsilon g)(n) \\ &= \underbrace{((f \oplus g \oplus \dots \oplus g) \odot g \odot \dots \odot g)}_{(\varepsilon-1)\text{times}}(n). \end{aligned} \right. \quad (25)$$

The result of the multiscale morphological filter is the impact-excluded signal which concentrates at low frequency range. In this study, the effective signal is the impact signal, thus we define the output signal of the multiscale morphological filter as the residual signal. The effective impact signal can be obtained by subtracting the output signal  $\mathbf{B}$  of the multiscale morphological filter from the original signal  $\mathbf{F}$ . Consequently, the effective impact signal  $\mathbf{X}$  can be expressed as

$$\mathbf{X} = \mathbf{F} - \mathbf{B}. \quad (26)$$

The mathematical morphology has attracted much attention in the signal and image processing communities, but it is still new in the rattle signal enhancing field. The scale  $\varepsilon$  and the length  $L$  of the structural element both affect the performance of the enhancing method. The rattle component in the signal usually exhibits impact characteristics. The kurtosis  $Kr$  is sensitive to the impact component in the signal.  $Kr > 3$  indicates that there are prominent rattle components in the signal. In this study, the kurtosis is introduced as the target of the optimization problem. When the kurtosis value of the enhanced signal reaches the maximum value, the corresponding scale and the length of the structural element are the optimal parameters for the filter. Kurtosis is the fourth-order central moment of the signal. For discrete signals  $x$ , the expression of kurtosis is

$$Kr = \frac{E(x - \mu)^4}{\sigma^4} = \frac{\frac{1}{n} \sum_{i=1}^n (x_i - \bar{x})^4}{\left( \frac{1}{n} \sum_{i=1}^n (x_i - \bar{x})^2 \right)^2}, \quad (27)$$

where  $\sigma$  is the standard deviation of the signal,  $\mu$  is the mean value, and  $E(x)$  represents the expected value.

## 4. Experimental validation for the proposed method

### 4.1. Experiments and data collection

In order to verify the proposed rattle signal denoising and enhancing methods vehicular test and component test were carried out to collect the noise signals. In this study, the brake caliper rattle noise was collected in the semi-anechoic chamber, and the in-vehicle background noise was also collected in the road test. The measured in-vehicle background noise is superimposed on the brake caliper rattle signal according to certain SNR ratios.

Figure 5 shows the set-up of the brake caliper rattle signal recording test, and Fig. 6 shows the layout of the in-vehicle background noise recording test. In these data recording tests, the free-field microphone of G.R.A.S. Sound & Vibration, the microphone calibrator of B&K, the quiet BSR energizer of MB Dynamics, and the eight-channel data acquisition system of Head Acoustics were used to collect noise samples. As shown in Fig. 5, the brake caliper assembly is installed on the test bench in line with the actual installation state in a vehicle to simulate the actual vertical vibration of the road excitation. The calibrated free-field microphone is aligned at the center of the brake caliper, and its front end is 300 mm away from the brake caliper. The acceleration sensors are placed near the installation point of the brake caliper to achieve the closed-loop control of the test bench. The excitation signal is the road excitation collected in vehicular road test, and a silent vibration exciter is used in the experiment to generate the signal. The in-vehicle background noise was collected on the rough road with speed of 40 km/h. As shown in Fig. 6, the placement of the calibrated free-field microphone meets the requirements of GB/T 18697-2002 ‘‘Acoustics – Method for measuring vehicle interior noise’’ (General Administration of Quality Supervision, 2002). The sampling frequency of these tests is 48 kHz, and the sampling length is 30 s. The collected signals will be segmented for further analysis.

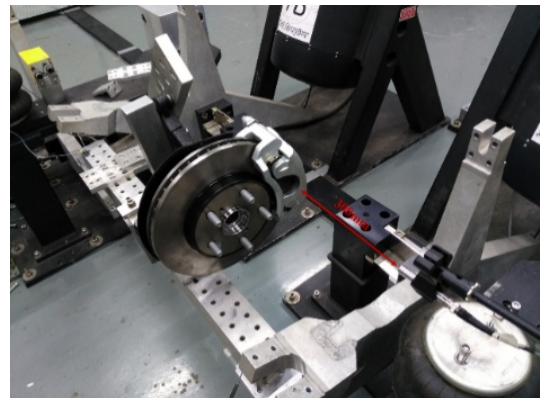


Fig. 5. Brake caliper rattle signal recording.



Fig. 6. In-vehicle background noise recording.

#### 4.2. Signal process

In order to simulate the real conditions in vehicle, the measured background noise is superimposed on the rattle signal according to certain SNR ratios. To show the effect of the algorithm proposed in this paper, the signal with a duration of 1 s is intercepted for analysis. Besides, the noise signal is standardized with the  $z$ -score standardization criterion. Figure 7 shows the curves of the original rattle signal and the signal superimposed with background noise (SNR = -30 dB). Figure 8 shows the Short-Time Fourier Transform of the original rattle signal and the synthesized signal. As can be seen in Fig. 7b, the rattle signal is completely masked by the background noise.

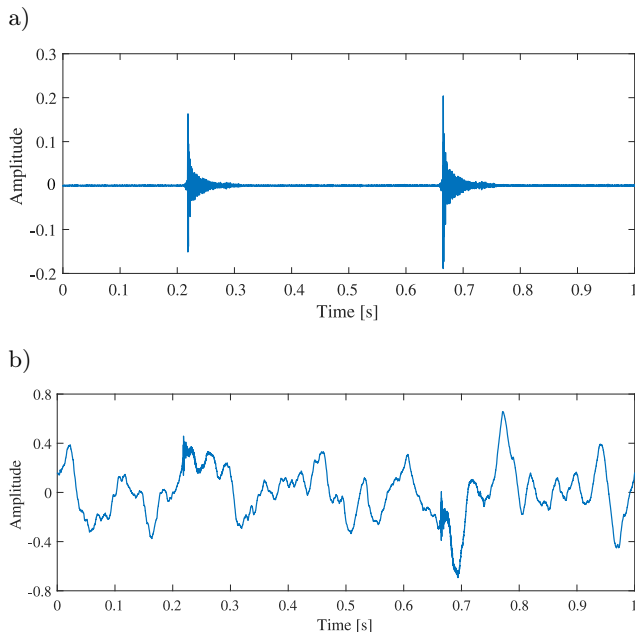


Fig. 7. The curves of the original rattle signal and the synthesized signal: a) original rattle signal, b) synthesized signal (SNR = -30 dB).

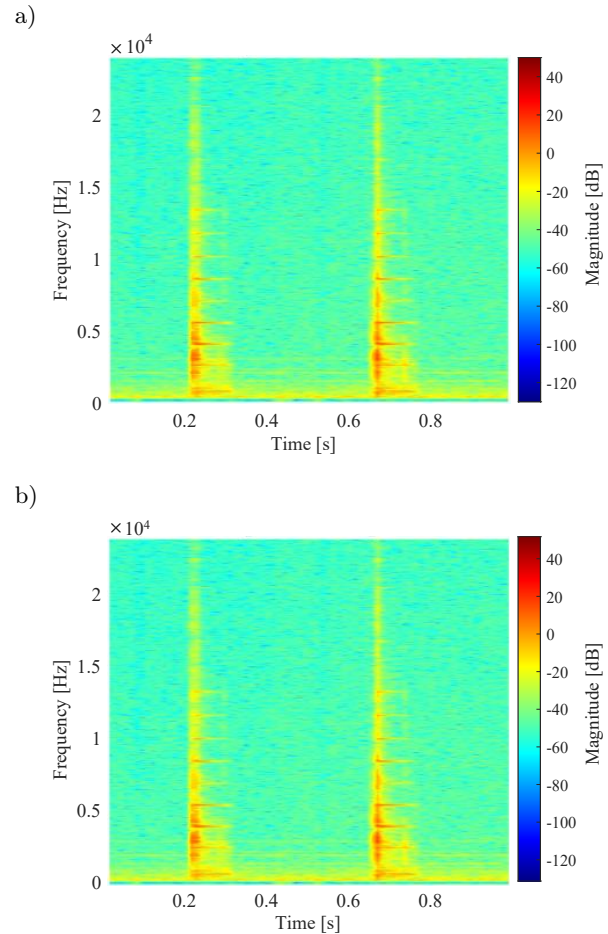


Fig. 8. The Short-Time Fourier Transform: a) original rattle signal, b) synthesized signal (SNR = -30 dB).

The synthesized signal is then processed by the improved wavelet packet threshold denoising method. After the wavelet packet decomposition, 36 wavelet packet coefficients are obtained. The wavelet packet thresholding method is performed on the wavelet packet coefficients. The comparison of the time-domain curves between the synthesized signal and the reconstructed signal is shown in Fig. 9. Significantly, the background noise is greatly reduced after the denoising process. It is evident that the improved wavelet packet thresholding method proposed in this paper can reduce the background noise to the greatest extent and retain the rattle components in the signal.

To achieve better SNR ratio, the multi-scale compound mathematical morphological filter is performed on the reconstructed signal. In this study, linear structural element is selected to filter the signal with multi-scale compound morphology filter.

The optimal scale  $\varepsilon$  of the filter and the length  $L$  of the structural element need to be determined first. The kurtosis value is introduced to perform a two-dimensional optimization of these two parameters. Set the value range of  $\varepsilon$  to [1, 10] and the value range of  $L$

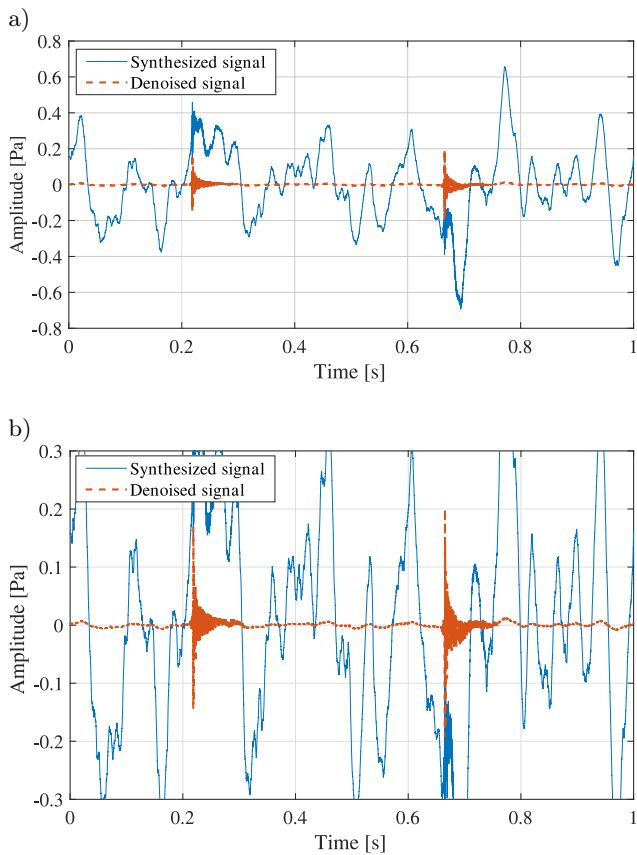


Fig. 9. The curves of the signals: a) full view, b) locally enlarged view.

to  $[1, 20]$ . Figure 10 shows a three-dimensional mapping surface with the filter scale  $\varepsilon$  as the  $x$  coordinate, the structural element length  $L$  as the  $y$  coordinate, and the kurtosis value  $Kr$  as the  $z$  coordinate. The highest point of the surface is the maximum kurtosis value. The point of the corresponding structural element length  $L = 1$  and filter scale  $\varepsilon = 4$  are the optimal parameters of the filter.

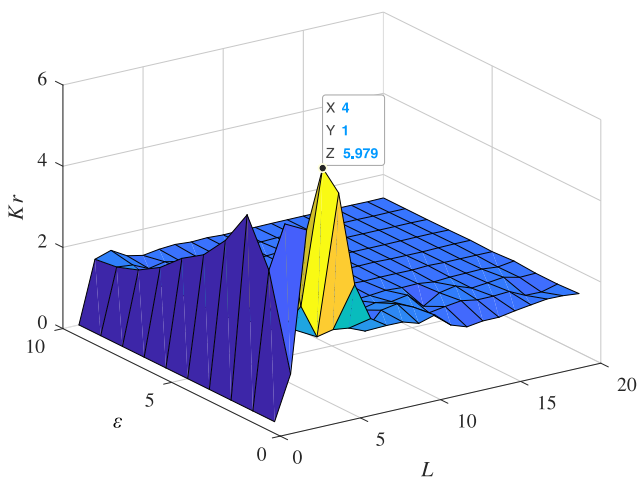


Fig. 10. The mapping surface between  $Kr$  and  $L$ ,  $\varepsilon$ .

Figure 11 shows the comparison of the time-domain curves between the synthesized signal and the enhanced signal. The SNR ratio of the enhanced signal shows a leaping promotion, which is 10.8105 dB.

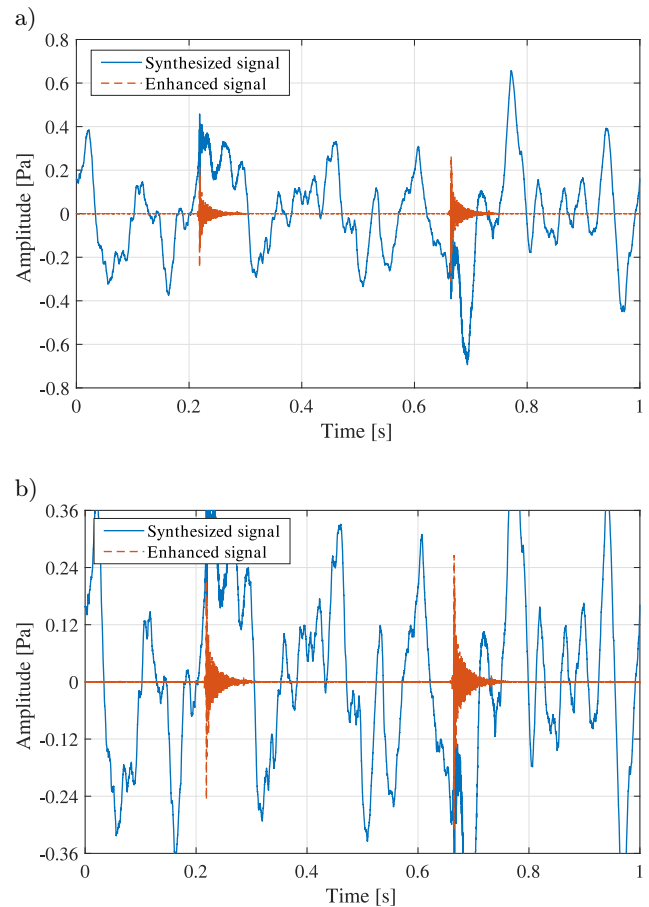


Fig. 11. The curves of the signals: a) full view, b) locally enlarged view.

Figure 12 shows the comparison of the time course of the original signal and after processing, and it can be seen that the proposed denoising and enhancing algorithms can reconstruct the rattle noise well. The Short-Time Fourier Transform of the enhanced signal is shown in Fig. 13. The interference components in the signal are effectively smoothed out. The low-frequency background is cleaned and the rattle components are enhanced sharply.

Figure 14 shows the performance of the denoising method between the proposed method and the traditional hard and soft thresholding wavelet packet denoising methods. Analyzing Fig. 14, the proposed method shows steady noise reduction performance compared with the other two methods. The proposed method has better denoising effects on signals with different SNR ratios, and both the SNR ratios and the RMSE values are significantly improved, which further validates superiority of the proposed method in this study.

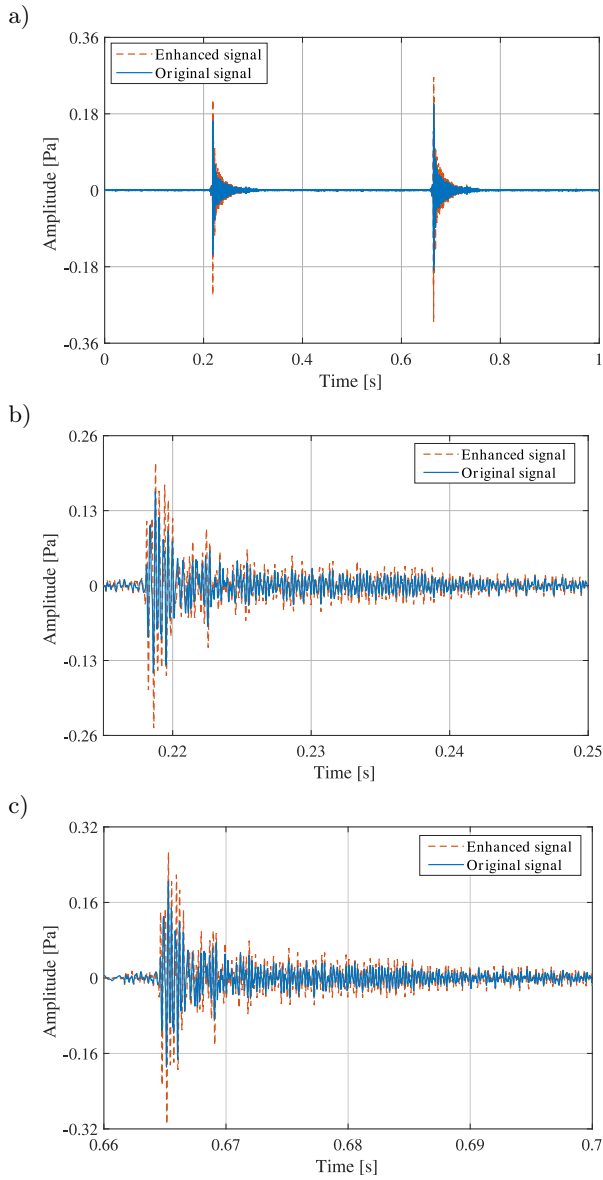


Fig. 12. The comparison of the time course between the original signal and the enhanced signal: a) full view, b) locally enlarged view of the first increase in amplitude, c) locally enlarged view of the second increase in amplitude.

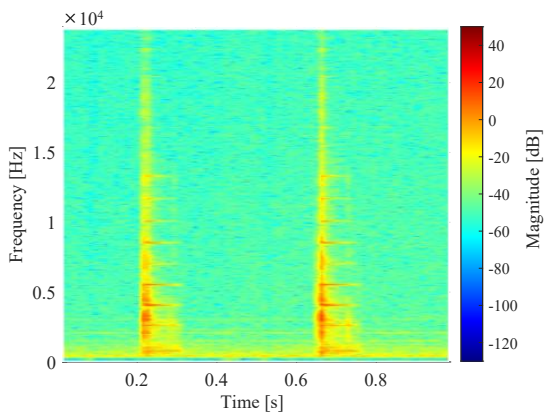


Fig. 13. The Short-Time Fourier Transform of the enhanced signal.

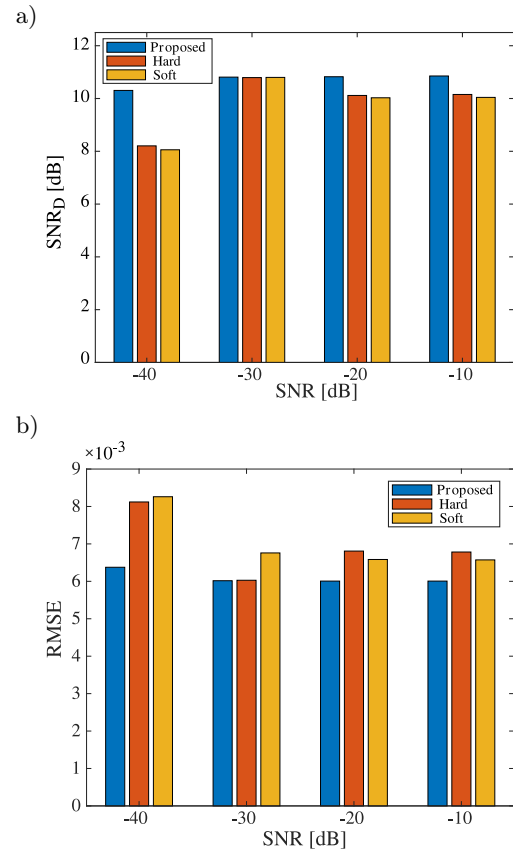


Fig. 14. The performance comparison of the denoising methods: a) SNR, b) RMSE.

### 5. Conclusion

In this paper, a rattle signal denoising and enhancing method was developed. The proposed method includes the signal denoising process based on the wavelet packet decomposition and the rattle component enhancing process based on the mathematical morphology filter. In the threshold denoising process, a wavelet packet decomposition structure that simulates the characteristics of auditory perception is proposed based on the critical frequency band. The information entropy is introduced to improve the wavelet packet threshold and the threshold function. The improved threshold and the threshold function can achieve adaptive thresholding, which can not only retain high-frequency rattle signals, but also effectively smooth out the noise signals. In the signal enhancing process, an enhancement algorithm based on a multi-scale compound morphological filter is proposed. Based on the kurtosis criterion, the scale of the filter and the length of the structural elements are optimized in two dimensions to obtain the best parameters of the filter. In order to verify the noise reduction and enhancement algorithm proposed in this paper, experiments were carried out including the in-vehicle background noise collection and in-lab brake caliper rattle signal

recording test. The background noise is superimposed on the rattle signal according to certain SNR ratios. Experimental results show that the proposed method demonstrates significant noise reduction and rattle signal enhancement effect. In the experiment, the sampling frequency is limited to 48 kHz, and a comparison of the signal spectra at different sampling frequencies will be made in the future research.

### Acknowledgements

This study was supported by the Open Fund of State Key Laboratory of Vehicle NVH and Safety Technology (NVH SKL-202004).

### References

- ADDISON P.S. (2002), *The Illustrated Wavelet Transform Handbook*, Boca Raton: CRC Press, doi: 10.1201/9781003040408.
- BI F., MA T., WANG X. (2019), Development of a novel knock characteristic detection method for gasoline engines based on wavelet-denoising and EMD decomposition, *Mechanical Systems and Signal Processing*, **117**: 517–536, doi: 10.1016/j.ymsp.2018.08.008.
- CHAUDHARI N., MOHAMMED R., RAGHAVENDRAN P. (2018), A disciplined approach to minimize rattle issues in automotive glove box assembly, *SAE Technical Paper*, 2018-01-1481, doi: 10.4271/2018-01-1481.
- CHEN W., SONG H. (2018), Automatic noise attenuation based on clustering and empirical wavelet transform, *Journal of Applied Geophysics*, **159**: 649–665, doi: 10.1016/j.jappgeo.2018.09.025.
- CHOI J.M., LYU S.J., SEOL Y.S., JUN I.K., YI C. (2013), A BSR analytical evaluation method considering the sound quality perception, *SAE Technical Paper*, 2013-01-1913, doi: 10.4271/2013-01-1913.
- DAVIES E.R. (2012), *Mathematical morphology*, [in:] *Computer and Machine Vision*, 4th ed., Boston: Academic Press.
- DONHO D.L. (1995), De-noising by soft-thresholding, *IEEE Transactions on Information Theory*, **41**(3): 613–627, doi: 10.1109/18.382009.
- DUAN T., LI P., CHEN S. (2021), Study of rattle noise in vehicle seat system under different excitation signals and loading conditions, *SAE Technical Paper*, 2020-01-5230, doi: 10.4271/2020-01-5230.
- GAO R.X., YAN R. (2011a), Continuous wavelet transform, [in:] *Wavelets: Theory and Applications for Manufacturing*, Gao R.X., Yan R. [Eds], Boston, Ma: Springer US, pp. 33–48.
- GAO R.X., YAN R. (2011b), Discrete wavelet transform, [in:] *Wavelets: Theory and Applications for Manufacturing*, Gao R.X., Yan R. [Eds], Boston, Ma: Springer US, pp. 49–68.
- General Administration of Quality Supervision (2002), *Gb/T 18697–2002: Acoustics – Method for measuring vehicle interior noise*, Standards Press of China Beijing, I.a.Q.o.t.P.s.R.o.C., Standardization Administration of The People’s Republic of China.
- HASHIM M.A., NASEF M.H., KABEEL A.E., GHAZALY N.M. (2020), Combustion fault detection technique of spark ignition engine based on wavelet packet transform and artificial neural network, *Alexandria Engineering Journal*, **59**(5): 3687–3697, doi: 10.1016/j.aej.2020.06.023.
- HUANG H.B., LI R.X., HUANG X.R., LIM T.C., DING W.P. (2016), Identification of vehicle suspension shock absorber squeak and rattle noise based on wavelet packet transforms and a genetic algorithm-support vector machine, *Applied Acoustics*, **113**: 137–148, doi: 10.1016/j.apacoust.2016.06.016.
- LI G., LIU X., TANG J., LI J., REN Z., CHEN C. (2020), De-noising low-frequency magnetotelluric data using mathematical morphology filtering and sparse representation, *Journal of Applied Geophysics*, **172**: 103919, doi: 10.1016/j.jappgeo.2019.103919.
- LI H., WANG R., CAO S., CHEN Y., HUANG W. (2016), A method for low-frequency noise suppression based on mathematical morphology, *Geophysics*, **81**(3): V159–V167, doi: 10.1190/geo2015-0222.1.
- LI H., WANG Y., WANG B., SUN J., LI Y. (2017), The application of a general mathematical morphological particle as a novel indicator for the performance degradation assessment of a bearing, *Mechanical Systems and Signal Processing*, **82**: 490–502, doi: 10.1016/j.ymsp.2016.05.038.
- LIANG L., CHEN S., LI P. (2020a), The evaluation of vehicle interior impact noise inducing by speed bumps based on multi-features combination and support vector machine, *Applied Acoustics*, **163**: 107212, doi: 10.1016/j.apacoust.2020.107212.
- LIANG L., CHEN S., LI P. (2021a), Experiment and evaluation study on rattle noise in automotive seat system, *International Journal of Automotive Technology*, **22**(2): 391–402, doi: 10.1007/s12239-021-0037-z.
- LIANG L., LI P., CHEN S. (2020b), Further study of the vehicle rattle noise with consideration of the impact rates and loudness, *SAE International Journal of Advances and Current Practices in Mobility-V129-99EJ*, **2**(4): 2285–2296, doi: 10.4271/2020-01-1261.
- LIANG L., LI P., CHEN S. (2021b), Novel method for identifying and assessing rattle noise on vehicle seat-belt retractors based on time-frequency analysis, *SAE Technical Paper*, 2021-01-5015, doi: 10.4271/2021-01-5015.
- PAN J., CHEN J., ZI Y., YUAN J., CHEN B., HE Z. (2016), Data-driven mono-component feature identification via modified nonlocal means and MEWT for mechanical drivetrain fault diagnosis, *Mechanical Systems and Signal Processing*, **80**: 533–552, doi: 10.1016/j.ymsp.2016.05.013.
- SERRA J. (2008), Advances in mathematical morphology: segmentation, [in:] *Advances in Imaging and Electron Physics*, Hawkes P. [Ed.], Elsevier, pp. 185–219, doi: 10.1016/S1076-5670(07)00004-3.

23. SHANNON C.E. (1948), A mathematical theory of communication, *The Bell System Technical Journal*, **27**: 379–423.
24. SHIN S.-H., CHEONG C. (2010), Experimental characterization of instrument panel buzz, squeak, and rattle (BSR) in a vehicle, *Applied Acoustics*, **71**(12): 1162–1168, doi: 10.1016/j.apacoust.2010.07.006.
25. TANG G., YAN X., WANG X. (2020), Chaotic signal denoising based on adaptive smoothing multiscale morphological filtering, *Complexity*, **2020**: 1–14, doi: 10.1155/2020/7242943.
26. TRAPP M., FANG C. (2012), *Automotive Buzz, Squeak and Rattle*, Butterworth-Heinemann: Oxford, doi: 10.1016/B978-0-7506-8496-5.01001-0.
27. WANG Y.S., LEE C.M., KIM D.G., XU Y. (2007), Sound-quality prediction for nonstationary vehicle interior noise based on wavelet pre-processing neural network model, *Journal of Sound and Vibration*, **299**: 933–947, doi: 10.1016/j.jsv.2006.07.034.
28. XING Y.F., WANG Y.S., SHI L., GUO H., CHEN H. (2016), Sound quality recognition using optimal wavelet-packet transform and artificial neural network methods, *Mechanical Systems and Signal Processing*, **66–67**: 875–892, doi: 10.1016/j.ymssp.2015.05.003.
29. XU G., WANG J., ZHANG Q., ZHANG S., ZHU J. (2007), A spike detection method in EEG based on improved morphological filter, *Computers in Biology and Medicine*, **37**(11): 1647–1652, doi: 10.1016/j.compbiomed.2007.03.005.
30. YANG G., LIU Y., WANG Y., ZHU Z. (2015), EMD interval thresholding denoising based on similarity measure to select relevant modes, *Signal Processing*, **109**: 95–109, doi: 10.1016/j.sigpro.2014.10.038.
31. YASLAN Y., BICAN B. (2017), Empirical mode decomposition based denoising method with support vector regression for time series prediction: a case study for electricity load forecasting, *Measurement*, **103**: 52–61, doi: 10.1016/j.measurement.2017.02.007.
32. YING L., JIN-YAN L. (2007), Experimental research on the rule of frequency-band derangement in wavelet packet transform, *2007 IEEE International Conference on Control and Automation*, 30 May–1 June 2007, pp. 3099–3102, doi: 10.1109/ICCA.2007.4376931.
33. YUE G.-D., CUI X.-S., ZOU Y.-Y., BAI X.-T., WU Y.-H., SHI H.-T. (2019), A Bayesian wavelet packet denoising criterion for mechanical signal with non-Gaussian characteristic, *Measurement*, **138**: 702–712, doi: 10.1016/j.measurement.2019.02.066.
34. ZHANG X., WAN S., HE Y., WANG X., DOU L. (2021), Teager energy spectral kurtosis of wavelet packet transform and its application in locating the sound source of fault bearing of belt conveyor, *Measurement*, **173**: 108367, doi: 10.1016/j.measurement.2020.108367.